

End-to-End Deep Visual Control for Mastering Needle-Picking Skills With World Models and Behavior Cloning

Hongbin Lin¹, Bin Li¹, Xiangyu Chu¹, Qi Dou², Yunhui Liu¹ and Kwok Wai Samuel Au¹

Abstract—Needle picking is a challenging surgical task in robot-assisted surgery due to the characteristics of small slender shapes of needles, needles’ variations in shapes and sizes, and demands for millimeter-level control. Prior works, heavily relying on the prior of needles (e.g., geometric models), are hard to scale to unseen needles’ variations. In addition, visual tracking errors can not be minimized online using their approaches. In this paper, we propose an end-to-end deep visual learning framework for needle-picking tasks where both visual and control components can be learned jointly online. Our proposed framework integrates a state-of-the-art reinforcement learning framework, Dreamer, with behavior cloning (BC). Besides, two novel techniques, i.e., Virtual Clutch and Dynamic Spotlight Adaptation (DSA), are introduced to our end-to-end visual controller for needle-picking tasks. We conducted extensive experiments in simulation to evaluate the performance, robustness, variation adaptation, and effectiveness of individual components of our method. Our approach, trained by 8k demonstration timesteps and 140k online policy timesteps, can achieve a remarkable success rate of 80%, a new state-of-the-art with end-to-end vision-based surgical robot learning for delicate operations tasks. Furthermore, our method effectively demonstrated its superiority in generalization to unseen dynamic scenarios with needle variations and image disturbance, highlighting its robustness and versatility. Codes and videos are available at <https://sites.google.com/view/dreamerbc>.

I. INTRODUCTION

Needle picking is a repetitive and time-consuming task during surgery where suturing needles are required to be picked up by suturing tools (e.g., instruments) before stitching. Automating such a task in robot-assisted surgery can greatly relieve surgeons’ workload. Although algorithms have been proposed to solve the needle-picking tasks [1]–[7], the proposed algorithms entail pose information of key objects (e.g., needles and grippers of suturing tools). A few works studied image-based visual servo methods where projected points of the key objects were tracked for control without the need for pose estimation in needle-insertion [8] and cutting tasks [9]. However, their methods require designing hand-crafted features on the key objects. Neither

This work was supported in part by the Chow Yuk Ho Technology Centre of Innovative Medicine, The Chinese University of Hong Kong, in part by the Multiscale Medical Robotics Centre, AIR@InnoHK, and in part by the Research Grants Council (RGC) of Hong Kong under Grants 14209118, 14209719, and 14211320. (Corresponding author: K. W. Samuel Au)

¹Hongbin Lin, Bin Li, Xiangyu Chu, Yunhui Liu and Kwok Wai Samuel Au are with Department of Mechanical and Automation Engineering, The Chinese University of Hong Kong, Hong Kong. {hongbinlin, binli}@link.cuhk.edu.hk; {xiangyuchu, yhliu, samuelau}@cuhk.edu.hk

²Qi Dou is with Department of Computer Science and Engineering, The Chinese University of Hong Kong, Hong Kong. qdou@cse.cuhk.edu.hk

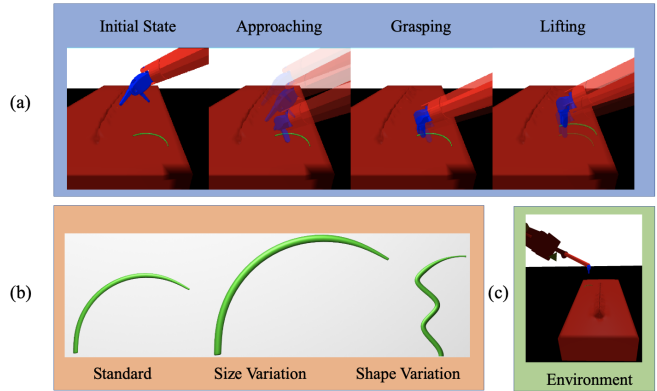


Fig. 1: (a) Canonical stages (initial state, approaching, grasping, and lifting) for needle-picking tasks in robot-assisted surgery. (b) Instances of needles, including a standard needle, a large needle representing size variation, and an irregular needle representing shape variation. (c) Simulation environment for needle picking.

the pose-estimation nor the feature-tracking methods are well adapted to unseen needles variations (e.g., shape or size variations shown in Fig. 1b) in needle-picking tasks due to the necessity of priors (e.g., geometric models of the key objects) and engineering efforts. Furthermore, visual components of their methods are designed or learned offline, and thus visual errors inside the controllers cannot be minimized online in a closed-loop form.

Remarkable achievements in vision-based robotic tasks, including dexterous manipulation [10] and robot grasping [11], were obtained by model-free end-to-end deep reinforcement learning (DRL), which can be effective solution candidates for needle-picking tasks due to their scalability in task variation. However, They required weeks of training on multiple real robots and distributed computation on multiple computers with high-end GPUs, which prevented most practitioners due to the high cost of robotic maintenance and lack of robotic and computational resources. Recent advances in the model-based end-to-end DRL demonstrate astounding data efficiency and low computational cost in video games and robotic tasks [12]–[14] while achieving competitive performances compared with the model-free DRL methods. World Model [15], which can predict action-condition future outcomes (including visual observations, rewards, etc.), was learned, largely reducing the amount of data needed through the interaction of robot and environment. Wu et al. [14] deployed a state-of-the-art (SOTA) world-model-based framework, Dreamer [13], to solve vision-based

manipulation tasks, where human-level policies for picking up large deformable objects (e.g., palm-sized sponges) were learned in real robots within 10 hours. However, geometric characteristics of needles (e.g., millimeter-level size and slenderness) pose challenges on both vision and control compared to large deformable objects when considering deploying Dreamer.

In this work, we are interested in endowing robots with needle-picking skills using end-to-end DRL. We propose a data-efficient DRL framework, DreamerBC, which integrates the SOTA framework Dreamer with BC. To the best of our knowledge, we are unable to find any end-to-end model-based DRL method for vision-based manipulation tasks of surgical autonomy. We focus on needle-picking tasks in this paper as the first step toward end-to-end model-based DRL for surgical autonomy. Our main contributions are:

- 1) A novel data-efficient RL framework that integrates the SOTA model-based RL framework, Dreamer, with BC for needle picking, where only RGB-D images, task-level states, and gripper states are observable for control;
- 2) Novel techniques (i.e., Dynamic Spotlight Adaptation and Virtual Clutch) that dramatically improve the performance of our end-to-end visual controller when picking needles;
- 3) Systematic evaluation for the efficiency of our method, showing our performance, robustness, variation adaptation, and effectiveness of individual components. We show our end-to-end deep visual control can adapt to the needle’s variations in shape and size.

II. RELATED WORKS

Liu et al. proposed to select grasping poses of a needle optimally for visual servo based on manipulability, dexterity, and torque metrics [1], [2]. Ettorre et al. first proposed a systematic framework for needle grasping without the assistance of angular positioners using visual servo approaches [3]. Sundaraesan et al. proposed a robust needle-grasping algorithm that was able to grasp needles in occluded configurations [4]. Chiu et al. [5] and Wilcox et al. [7] focused on needle re-grasping, where a robotic arm was required to hand over its grasped needle to another robotic arm. Chiu et al. achieved rapid motion planning by BC-integrated DDPG in [16], where trajectories generated by sampling-based motion planning methods served as demonstrations for speeding up the learning process. Wilcox et al. studied re-grasping modified occluded needles where techniques of deep learning, active sensing, and visual servo were applied. Xu et al. trained DRL methods in simulation, followed by transferring trained policies to real robots for multiple surgical tasks including needle picking, needle re-grasping, and some other tasks [6]. Zhong et al. applied active deformation control [8] to needle-insertion tasks based on the observation of tracked hand-crafted feature points. However, the methods mentioned above are required to track either poses or hand-crafted feature points of needles and/or robotic arms, and the tracking error cannot be minimized online in a closed

TABLE I: Comparison of related methods for visual control in surgical tasks

Categories	Related Works	Pose Estimation Free	Geometric Prior Free	Variation Adaptation
Pose-Estimation Methods	[1]–[7]	✗	✗	✗
Handcrafted-Feature Methods	[8], [9]	✓	✗	✗
End-to-End Model-based Deep Visual Control	Ours	✓	✓	✓

loop. In addition, these methods heavily rely on the prior of needles (e.g., the geometric model of needles), preventing the practitioners from applying their methods to unseen task variations (e.g., variations of needle shape and size). Table I shows an overview of the comparison of the related works.

III. PROBLEM DESCRIPTION

We focus on solving needle-picking tasks for surgical robotics, where a needle on a plane is required to be picked up by a robotic arm. The initial poses of the needle and the gripper are random. RGB-D images I_t from a monocular camera are observed at time t . Discrete commands can be sent for servoing the robotic arm incrementally. Specifically, the robotic gripper can be driven translationally (along X, Y, and Z axes for Δd mm), and rotationally (along the normal axis of the plane for $\Delta\theta$ Deg) in both positive and negative direction w.r.t. a fixed world frame; The jaw of the gripper can be opened and closed by a toggling command; All commands are decoupled, resulting in discrete commands a_t in a 9-element discrete set A at time t . The tasks of needle picking have a finite task horizon T . We define the task as successful if the needle is picked up by the gripper. The goal of our work is to develop a control policy that maps from historical observed images to control actions. We assume that 1) the robotic arm will not exceed joint limits during the task and 2) the needle and the gripper cannot be fully occluded.

IV. PRELIMINARIES

A. Problem Formulation

We model the needle-picking task as a discrete-time partially observable Markov Decision Process (POMDP) with discrete action space, which can be formally described as a 7-tuple $(S, A, T, R, \Omega, O, \gamma)$. The elements in the 7-tuple are defined as follows: S is a set of partially observable states; $R(s, a) : S \times A \rightarrow \mathbb{R}$ is a reward function; T is a set of conditional transition probabilities between states; O is a set of conditional observation probabilities; $\gamma \in [0, 1]$ is the discount factor; Ω is the observation and A is a set of action defined in Section III. The goal is to learn a control policy π that maximizes its expected future discounted reward $\mathbb{E}_\pi[\sum_{i=t}^T \gamma^{i-t} r_i]$, where r_i is the reward at time i and t is the current time.

B. Dreamer

The Dreamer framework consists of 2 components: a world model and an actor policy. The world model, targeting model POMDP under environment, learns from offline experience data $\mathcal{D} = \{o_0, a_0, r_0, \gamma_0, \dots, o_T, a_T, r_T, \gamma_T\}$ sampled from the experiences of the actor policy using a replay buffer \mathcal{R} , while the actor policy is improved by merely simulated rollouts based on the learned world model, and serves as a rollout policy interacting with the environment to generate offline experiences for the world model learning.

In particular, the world model can encode sensory observation o_t to compact-dimension state s_t , where images and scalar signals are encoded by Convolution Neural Network (CNN) and Multi-Layer Perceptron (MLP), respectively. In addition, the dynamics of latent encoded states are modeled by Recurrent State-space Model (RSSM). In particular, the compact state s_t is concatenated by a deterministic state h_t and a stochastic state z_t as $s_t = [h_t, z_t]$. Gated Recurrent Unit (GRU) is used to model the dynamics of deterministic latent state $h_t = f_\phi(h_{t-1}, z_{t-1}, a_{t-1})$, while the prior and posterior stochastic states are modeled by Gaussian MLP $\hat{z}_t \sim p_\phi(\hat{z}_t|h_t)$ and $z_t \sim q_\phi(z_t|h_t, o_t)$, respectively. Image, reward, and discount are predicted by Gaussian MLP as $\hat{o}_t \sim p_\phi(\hat{o}_t|h_t, z_t)$, $\hat{r}_t \sim p_\phi(\hat{r}_t|h_t, z_t)$, $\hat{\gamma}_t \sim p_\phi(\hat{\gamma}_t|h_t, z_t)$, respectively. For the actor policy, the actor-critic algorithm was used to improve the policy, where an actor $p_\psi(\hat{a}_t|\hat{z}_t)$ and a critic $v_\xi(\hat{z}_t)$ are used to predict the action and the value, respectively. The world model is designed as follows:

$$\mathcal{L}_\phi = \mathcal{L}_\phi(\mathcal{D}) = \mathbb{E}_{(o_t, r_t, \lambda_t) \sim \mathcal{D}} \left[\sum_{t=1}^T -\ln p_\phi(o_t r_t \gamma_t | h_t, z_t) + \beta KL(q_\phi || p_\phi) \right], \quad (1)$$

where KL is a KL divergence loss and β is a scaling factor for the loss. The critic network tracks the λ -return V_t based on a mean square loss as:

$$\mathcal{L}_\xi = \mathcal{L}_\xi(\rho) = \mathbb{E}_{p_\phi, p_\xi, s_0 \sim \rho} \left[\frac{1}{2} \sum_{t=1}^{H-1} (v_\xi(\hat{z}_t) - sg(V_t))^2 \right], \quad (2)$$

where $sg(\cdot)$ denotes the stop gradient function, and ρ is a probability distribution of the initial state representing uniformly sampling from experienced states in \mathcal{D} . The actor policy improves the policy performance using the Reinforce algorithm and encourages training exploration using entropy regularization, where the loss of the policy improvement is

$$\mathcal{L}_\psi = \mathcal{L}_\psi(\rho) = \mathbb{E}_{p_\phi, p_\psi, s_0 \sim \rho} \left[\sum_{t=1}^{H-1} \underbrace{-\ln p_\psi(\hat{a}_t | \hat{z}_t) sg(V_t - v_\xi(\hat{z}_t))}_{reinforce} - \underbrace{\eta H[a_t | \hat{z}_t]}_{entropy} \right], \quad (3)$$

where H is the loss of an entropy regularizer and η is a scaling weight for the regularizer. Details of the Dreamer framework can be found in [13].

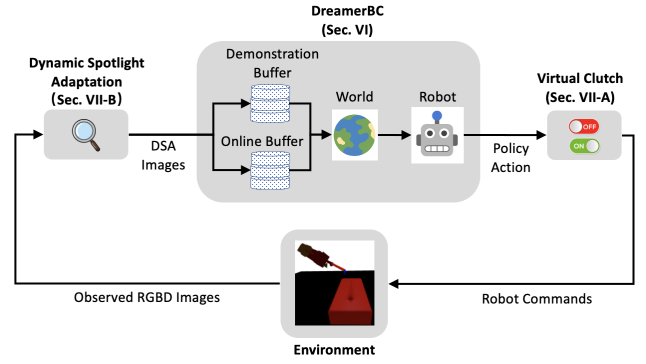


Fig. 2: An overview of our visual learning pipeline. Experiences of our robot actor are collected from the needle-picking environment. Observed RGB-D images of the collected experiences are preprocessed by Dynamic Spotlight Adaptation, followed by adding the preprocessed experiences to data buffers, a buffer for demonstration, and a buffer for the online actor policy. A world model learns from the data buffers and generates simulated rollouts for policy learning. Robot commands are controlled by Virtual Clutch, which switches between idle commands and learned policy commands.

V. OVERVIEW

In this section, we summarize the learning pipeline of our deep visual control for needle picking (see Fig. 2). Through a small set of demonstrations, our learning method (See Section VI), which integrates Dreamer with BC, can effectively solve the POMDP problem with large observation space and sparse delayed reward. We propose Virtual Clutch (see Sec. VII-A) to address the issue of poor state estimation in the first few steps of a rollout due to sub-optimal initial guess value. Our proposed Dynamic Spotlight Adaptation (See Sec. VII-B), targeting to solve the visual problem of needle picking, can effectively extract information of key objects from high-dimensional RGB-D images and represent it on a compact image space ($64 \times 64 \times 3$).

VI. DREAMERBC: INTEGRATING WORLD MODELS AND BC

We utilize a set of suboptimal expert experiences \mathcal{D}_E , which is gathered by either human demonstration or hand-engineered program, for the learning of both the world model and the actor in the Dreamer framework. In particular, a world model loss, that minimizes the prediction error of POMDP dynamics based on the expert experiences, is formulated by replacing the policy experiences \mathcal{D} in (1) with expert data \mathcal{D}_E as

$$\mathcal{L}_\phi^{BC} = \mathcal{L}_\phi(\mathcal{D}_E); \quad (4)$$

For actor learning, initial states are reset to sampled demonstration states so that the agent can be exposed to states with high rewards. To this end, the critic loss in (2) can be reformulated as

$$\mathcal{L}_\xi^{BC} = \mathcal{L}_\xi(\rho_E), \quad (5)$$

where ρ_E is the initial state distribution where initial states are sampled uniformly from \mathcal{D}_E ; For actor loss, besides

Algorithm 1 DreamerBC

Input: Task environment env , batch size M , batch length N , imagine horizon H , number of gradient updates K , expert experience \mathcal{D}_E , pre-training steps L_{pre} , maximum training steps L , gradient update steps L_{every} , learning rate l_ϕ for world model, l_ξ for critic and l_ψ for actor.

Output: Parameters ϕ , ξ , and ψ

- 1: Randomly initializes neural networks: $p_\phi, q_\phi, v_\xi, v'_\xi, p_\psi$.
 - 2: Initialize replay buffers $\mathcal{R} \leftarrow \mathcal{D}_E, \mathcal{R}_E \leftarrow \emptyset$
 - 3: Track target critic network: $\xi' \leftarrow \xi$.
 - 4: Pretrain by Calling $TrainUpdate()$ for L_{pre} times.
 - 5: **while** training step $i \leq L$ **do**
 - 6: $j \leftarrow 0$.
 - 7: **while** $j \leq L_{every}$ **do**
 - 8: Reset env and get $o_0, t \leftarrow 0 \mathcal{D}' \leftarrow \emptyset$.
 - 9: **while** env is not terminated **do**
 - 10: $h_t = f_\phi(h_{t-1}, z_{t-1}, a_{t-1})$.
 - 11: $z_t \sim q_\phi(z_t | h_t, o_t)$.
 - 12: $a_t \leftarrow \hat{a}_t = q_\psi(o_t | h_t, z_t)$.
 - 13: Perform action a_t on env and get r_{t+1}, o_{t+1} .
 - 14: Store transition $(o_t, a_t, r_{t+1}, o_{t+1})$ to \mathcal{D} .
 - 15: $i \leftarrow i + 1, j \leftarrow j + 1, t \leftarrow t + 1$.
 - 16: Load \mathcal{D} to replay buffer \mathcal{R} .
 - 17: Call $TrainUpdate()$ for K times.
 - 18: **procedure** TRAINUPDATE():
 - 19: Sample a $M \times N$ batch from \mathcal{R}_E randomly.
 - 20: Calculate \mathcal{L}_ϕ^{BC} in (4) and its gradient $\nabla \mathcal{L}_\phi^{BC}$.
 - 21: $\phi \leftarrow \phi - l_\phi \nabla \mathcal{L}_\phi^{BC}$.
 - 22: $\rho_E \leftarrow$ State distribution in the sampled batch.
 - 23: Imagine H rollouts given $p(\phi), p(\psi)$, and ρ_E .
 - 24: Calculate \mathcal{L}_ξ^{BC} in (5), \mathcal{L}_ψ^{BC} in (6) and their gradients $\nabla \mathcal{L}_\xi^{BC}, \nabla \mathcal{L}_\psi^{BC}$.
 - 25: $\xi \leftarrow \xi - l_\xi \nabla \mathcal{L}_\xi^{BC}$.
 - 26: $\psi \leftarrow \psi - l_\psi \nabla \mathcal{L}_\psi^{BC}$.
 - 27: **if** \mathcal{R} is not \emptyset **then**
 - 28: Sample a $M \times N$ batch from \mathcal{R} randomly.
 - 29: Calculate \mathcal{L}_ϕ in (1) and its gradient $\nabla \mathcal{L}_\phi$.
 - 30: $\phi \leftarrow \phi - l_\phi \nabla \mathcal{L}_\phi$.
 - 31: $\rho \leftarrow$ State distribution in the sampled batch.
 - 32: Imagine H rollouts given $p(\phi), p(\psi)$, and ρ_E .
 - 33: Calculate \mathcal{L}_ξ in (2), \mathcal{L}_ψ in (3) and their gradients $\nabla \mathcal{L}_\xi, \nabla \mathcal{L}_\psi$.
 - 34: $\xi \leftarrow \xi - l_\xi \nabla \mathcal{L}_\xi$.
 - 35: $\psi \leftarrow \psi - l_\psi \nabla \mathcal{L}_\psi$.
-

resetting to sampled demonstration states, a BC loss, that trains the actor to regress actions of expert experience, is combined with the actor loss in (3), which is formulated as

$$\mathcal{L}_\psi^{BC} = \eta_a \mathcal{L}_\psi(\rho_E) - \eta_{bc} \underbrace{\mathbb{E}_{p_\phi, p_\xi, s_0 \sim \rho_E} \ln p_\psi(a_t | \hat{z}_t)}_{BC}, \quad (6)$$

where η_a and η_{bc} are non-negative constants to scale the effect of actor improvement and BC, respectively. Algorithm 1 shows the proposed algorithm DreamerBC.

VII. END-TO-END DEEP VISUAL CONTROL FOR NEEDLE PICKING

In this section, we will show how to deploy our DreamerBC framework to needle-picking tasks. We will elaborate on two proposed techniques, Dynamic Spotlight Adaptation and Virtual Clutch, that dramatically improve image representation and mitigate the poor initial state estimation, respectively. Finally, we will introduce a task-level Finite State Machine for needle picking.

A. Virtual Clutch for Visual Controller

The initial prior state $\hat{s}_0 = [h_0, \hat{z}_0]$ in a rollout is set to an initial guess value (e.g., a zero matrix in [12]) during training and evaluation. Although the estimation error between prior and posterior states gradually shrinks as the timestep of a rollout increases, the controller of Dreamer performs poorly for the first few steps due to large estimation errors, leading to catastrophic results, (See the results in our ablation study in the later Sec. VIII-E).

We propose a simple technique, Virtual Clutch, to solve this issue. Our inspiration is from vehicle clutch design where vehicles can only be driven when the clutch is closed. Similarly, the control output of our controller a_t^c is determined by a timestep-dependent clutch as

$$a_t^c = \begin{cases} a_t, & t \geq H_{clutch} \\ a_{idle}, & t < H_{clutch}, \end{cases} \quad (7)$$

where a_{idle} is an idle action command that keeps the joint positions of the robot arm unchanged, H_{clutch} is a positive constant determining the timestep that starts to close the virtual clutch, and a_t is the action from the learned agent policy. Fig. 4 shows the detailed illustration for Virtual Clutch.

B. Dynamic Spotlight Adaptation for Image Representation

Learning the visual component of Dreamer for needle picking is challenging because: (a) the standard Dreamer framework used down-sampled low-resolution images due to limitations of computational complexity and model capacity, leading to degradation of geometric and pose-related information, especially for the needle-picking tasks where the needles are tiny and slender; (b) scene background can be noisy and variational, resulting in increasing complexity of representation learning.

We propose Dynamic Spotlight Adaptation (DSA) for image representation, targeting to solve the aforementioned problems. In particular, we first segment the region of interest of key objects (i.e., the needle and the gripper) with our color-based scripted program, where the binary image masks, M_n and M_g , are obtained for the needle and the gripper, respectively. Then, the depth-channel image matrix of the observed image dI is segmented by the predicted masks for both needle and gripper as

$${}^dI_g = {}^dI \odot M_g, \quad {}^dI_n = {}^dI \odot M_n, \quad (8)$$

where \odot is a dot product operator, and dI_g and dI_n are the corresponding segmented matrices for the gripper and needle,

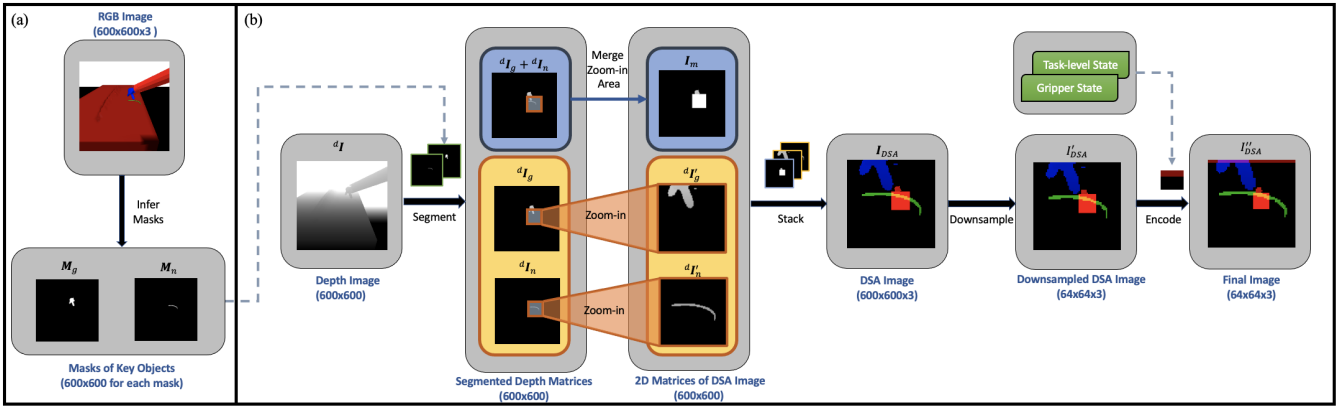


Fig. 3: Pipeline of Dynamic Spotlight Adaptation (DSA) for needle picking. (a) shows that segmented masks of key objects are inferred by a color-based scripted program based on RGB images. In (b), depth images are segmented by the inferred masks. 2D matrices of DSA images can be obtained by zooming in the segmented depth matrices for a needle and a gripper, followed by merging the zoom-in area with the segmented depth image of key objects. We stack the 2D matrices to a 3D DSA image, followed by downsampling. The final image is obtained by merging the resultant downsampled image with the image encoding of task-level states and gripper states.

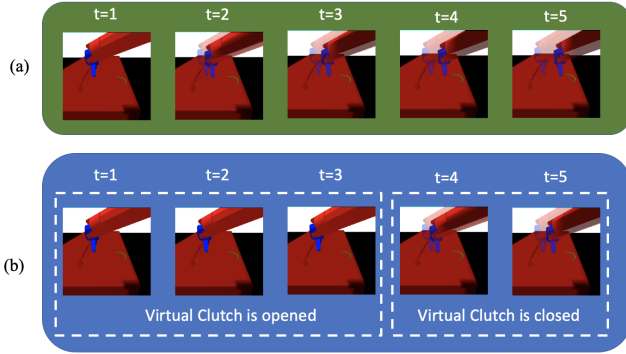


Fig. 4: Schematic illustration for Virtual Clutch. (a) shows the first 5 steps of a rollout when Virtual Clutch is not applied to our visual controller. (b) shows the corresponding 5 steps after applying Virtual Clutch ($H_{clutch} = 3$).

respectively. The segmented matrices, dI_g and dI_n in (8), are further zoomed in, where the segmented matrices are cropped by a bounding square box \mathbf{B} , followed by resizing the resultant cropped matrices as

$${}^dI'_g = f_{rs}(f_{crop}({}^dI_g, \mathbf{B})), \quad {}^dI'_n = f_{rs}(f_{crop}({}^dI_n, \mathbf{B})), \quad (9)$$

where f_{crop} and f_{rs} are the image crop and resize function, respectively; \mathbf{B} is the square bounding box which has the same center coordinates with the bounding box of dI_n and a side length $b \in [1, +\infty)$ times the maximum side length of the bounding box, considering leaving image margins; the resultant matrices ${}^dI'_g, {}^dI'_n$ correspond to dI_g and dI_n , respectively. Besides, an additional matrix I_m that contains mixed information of bounding box \mathbf{B} , the un-zoomed matrices of dI_g and dI_n is formulated as

$$I_m = f_{rs}(f_{clip}(\mathbf{B} + {}^dI_g + {}^dI_n)), \quad (10)$$

where f_{clip} is a clip function that saturates the input value to

the range $[0, 255]$, which is the range for an 8-bit unsigned integer. We stack three 2-D matrices, ${}^dI'_g, {}^dI'_n$ and I_m , to a 3-D matrix I_{DSA} for DSA as

$$I_{DSA} = \begin{bmatrix} I_m & {}^dI'_n & {}^dI'_g \end{bmatrix}. \quad (11)$$

Finally, we obtain the final image I''_{DSA} for our image representation by downsampling I_{DSA} , followed by adding image encoding of gripper states and task-level states I_e to the downsampled image I'_{DSA} as

$$I'_{DSA} = f_{rz}(I_{DSA}), \quad I''_{DSA} = I'_{DSA} + I_e, \quad (12)$$

where $I'_{DSA}, I''_{DSA}, I_e \in \mathcal{R}^{64 \times 64 \times 3}$. Fig. 3 illustrates the pipeline of DSA in detail.

C. Task-level Finite State Machine

We design a Finite State Machine (FSM) that directly determines task termination and reward assignment. The task-level states in FSM are defined as:

- Succeeded Terminated State: The needle is successfully grasped. In this state, the reward is 1 and the task is terminated.
- Failed Terminated State: The task failed due to the limit of task horizon T . In such a case, the reward is -0.1 and the task is terminated.
- Failed Non-terminated State: The task failed due to exceeding the workspace. In such a case, the reward is -0.01 and the task is not terminated. In addition, the actor action will be replaced by a_{idle} for the control output.
- In-progress State. The task is performed in progress. The reward is -0.001 and the task is not terminated.

VIII. EXPERIMENTS

Extensive experiments were carried out in the simulation, aiming to answer the following questions:

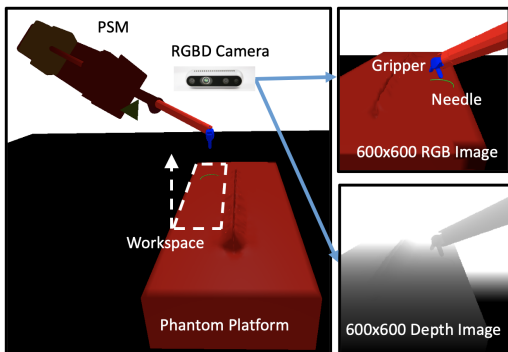


Fig. 5: Experiment setup.

- How is the performance of our method compared to the SOTA framework?
- Can our method adapt to unseen task variations?
- Is our method robust to unseen noises and disturbances?
- How effective are the individual components of our methods?

We start with introducing the experiment setup of simulation, followed by elaborating on the studies of performance, variation adaptation, robustness, and ablation.

A. Experiment Setup

We conducted experiments on the simulation platform of 2021-2022 AccelNet Surgical Robotics Challenge [17], which provided high-fidelity simulation, standardized problem definitions, and evaluations for benchmarking autonomous suturing (See Fig. 5). We developed our simulation code based on our previous work [18], which ranked first among all competitors. The dimension of the workspace was $40mm \times 60mm \times 30mm$; The initial poses of both the needle and the gripper were randomized along $x - y$ planes within our workspace. A third-person camera provided $600 \times 600 \times 4$ RGB-D images for visual feedback. Synthetic colors, (blue for the gripper, green for the needle, and red for the context), were used to reduce the difficulty of our color-based segmentation since segmentation is beyond the focus of this paper. The success rate was chosen as the key index of our evaluation, similar to that of [7]. Rollouts beyond our assumptions in the evaluation were neglected. For each training of our method and baselines, the maximum training timesteps L was 140000; 20 evaluation rollouts were carried every 2000 training timestep for the evaluation of the success rate; 8000 timesteps of demonstrations, (approximately 400 rollouts), were pre-filled using a script developed in our previous work [18]; The task horizon T for training and evaluation is 100; Each training of the experiment was run on a workstation with an 8 Gigabyte or higher GPU for 3 days. Detailed hyperparameters can be found in Appendix I.

B. Performance Study

We compared our method with the SOTA model-based framework, Dreamer [13], in simulation. To keep the image observation space the same as ours for a fair comparison, the original RGB-D images were transformed into mixed

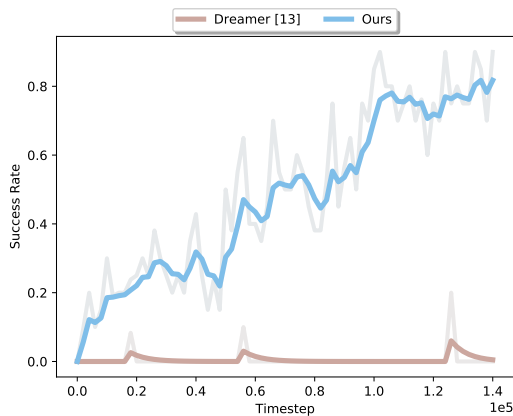


Fig. 6: Success rate in the evaluation of our performance study. Curves are smoothed by Exponential Moving Window with a 0.7 smoothing factor.

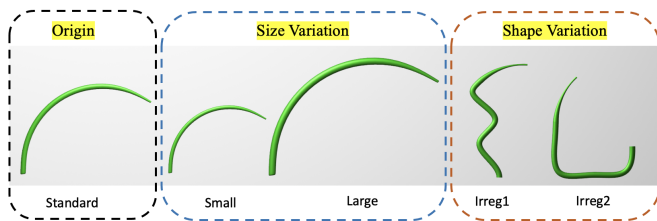
images with 3 channels, where one channel was obtained by the weighted summation of the original red and blue channels, and the remaining two channels were the original blue and depth channels. The resultant mixed images were downsampled to $64 \times 64 \times 3$ images as [13], [14] suggested. Scalar signals, (i.e., task-level states and gripper states), were encoded by MLP. The remaining training settings for the baseline were kept consistent with our approach.

Fig. 6 shows the results of the performance study. Our method converged after 134k training timesteps, reaching 80% success rate in the evaluation. Compared to our method, the Dreamer baseline had not yet converged after 140k training timesteps. Although we observed incremental improvement at around 20k, 60k, and 125k training timesteps, the success rate was extremely low for most of the training timesteps. In the performance study, our method demonstrated higher data efficiency when solving the POMDP of the needle-picking tasks.

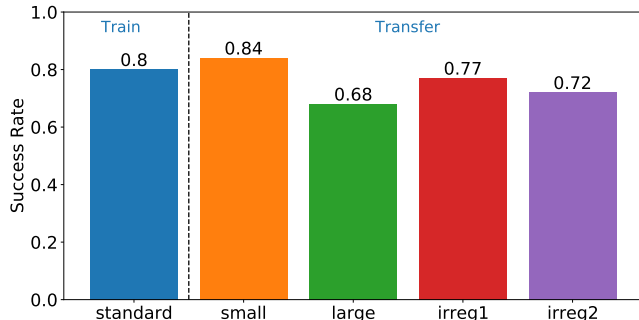
C. Variation Adaptation Study

We designed a wide variety of needles for the study of variation adaptation (see Fig. 7a). The needle in AccelNet Surgical Robotics Challenge [17] served as the standard needle. For the size variation, a small needle and a large needle were obtained by scaling the standard needle by the factor of 0.75 and 1.3, respectively. For the shape variation, we designed two irregular needles the same size as the standard needle. Note that our visual controller was only trained on the standard needle, and then transferred directly to grasp the unseen needles with shape or size variations.

Fig. 7b shows the performance of our trained model applied to unseen needles. The standard needle served as the baseline. We observe that our model achieved a higher success rate of 84% for grasping small needles because of its higher error tolerance, and achieved similar performance in grasping varied irregular shape needles with the same size compared to the baseline. Although the grasping larger size needle requires a more accurate claw pose, as thicker width reserves less space for opened claw with a certain width



(a) Schematic illustration of needle variation



(b) Performance of variation adaptation

Fig. 7: Study of variation adaptation. In (a), we show needle instances for size variation and shape variation. In (b), our controller was first trained based on the standard needle and then transferred to unseen needles with variations. For each needle, the success rate was evaluated with 100 rollouts.

which means less error tolerance, our method can still obtain a success rate of up to 68%. The above promising results demonstrated our model can be efficiently adapted to unseen needle variants.

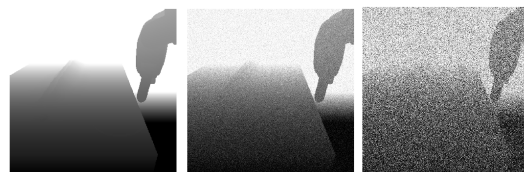
D. Robustness Study

We evaluated the robustness of our method quantitatively and qualitatively. For the quantitative evaluation of robustness, we transferred our trained controller to unseen environments with two different noise levels of depth images. In particular, noises were added to observed depth images. To obtain the noise distribution, the unit Gaussian distribution was scaled by a factor of $255 \cdot \eta_n$ (See Fig. 8a). As Fig 8b shows, our controller successfully transferred to the unseen environments with a low noise level ($\eta_n = 0.1$), which is similar to that of real RGB-D cameras. Even in the environment with an unrealistic high noise level ($\eta_n = 0.5$), the reduction in success rate was 19% compared to our baseline ($\eta_n = 0$), indicating our method has a strong robustness to depth image noises. For the qualitative evaluation of robustness, external disturbances were applied to the needle. Our learned controller was able to grasp the dynamic needle due to perturbation and learn to re-grasp within the task. Qualitative results can be found in our supplementary video.

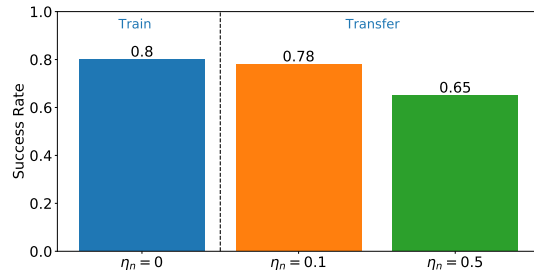
E. Ablation Study

We evaluated the effectiveness of individual components in the ablation study, where ablative baselines are:

- 1) Removal of BC (No BC). In this baseline, we set η_{bc} to zero to remove the effect of BC.



(a) Depth images under different noise levels



(b) Performance in robustness study

Fig. 8: Robustness study. In (a), we show 3 different noise levels for depth images. In (b), our controller was first trained in the environment with noise-free depth images ($\eta_n = 0$) and then transfer to environments with noisy depth images ($\eta_n = 0.1$ and $\eta_n = 0.5$). For each baseline, the success rate was evaluated with 100 rollouts.

- 2) Removal of actor gradients (No Actor Grad). We set η_a to zero to remove the effect of actor improvement.
- 3) Removal of DSA (No DSA). We replaced the DSA images with the mixed images in the Dreamer baseline.
- 4) Removal of Virtual Clutch (No Virtual Clutch). H_{clutch} was set to zero to remove the effect of Virtual Clutch.

Fig. 9 shows the evaluated success rate during training in our ablation study. The success rate of our method was significantly higher compared to No BC and No Actor Grad, demonstrating the efficient policy learning of our method using the mixed effect of actor improvement and BC. The learning of No Virtual Clutch was more unstable compared to ours as its success rate dropped to zero in the course of training. The introduction of Virtual Clutch, on the other hand, effectively eliminates the instability effect due to the suboptimality of the initial prior state, resulting in a steady increase in the success rate of the training process. Our method converged faster and performed better than No DSA, indicating that our image representation using DSA was more efficient for the learning of end-to-end deep visual control in needle-picking tasks.

IX. CONCLUSION AND DISCUSSION

In this paper, we proposed DreamerBC, an end-to-end data-efficient DRL framework for needle-picking that combines Dreamer with BC. Two novel techniques, DSA and Virtual Clutch, were deployed to our end-to-end deep visual controller to improve the efficiency of our controller. Extensive experiments were carried out to evaluate the performance, variation adaptation, robustness, and efficiency of individual components of our method.

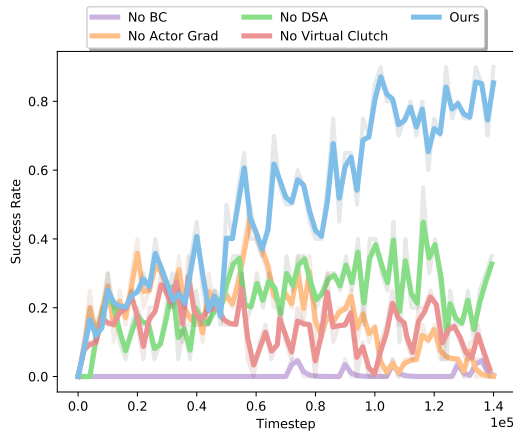


Fig. 9: Success rate in the evaluation of our ablation study. Curves are smoothed by Exponential Moving Window with a 0.3 smoothing factor.

In our future work, we will mainly explore in the following directions: 1) Improving the success rate of our method for needle picking; 2) Accelerating the speed of data generation in simulations; 3) Parallel computation for data generation and model training for DreamerBC similar to [14]; 4) Deploying our method to other surgical tasks and the robotic manipulation tasks beyond the scope of surgical autonomy.

X. ACKNOWLEDGEMENT

Thanks for the technical discussion with Adnan Munar and Juan Barragan Noguera on the simulation.

REFERENCES

- [1] T. Liu and M. C. Çavuşoğlu, “Optimal needle grasp selection for automatic execution of suturing tasks in robotic minimally invasive surgery,” in *2015 IEEE International Conference on Robotics and Automation (ICRA)*. IEEE, 2015, pp. 2894–2900.
- [2] T. Liu and M. C. Cavusoglu, “Needle grasp and entry port selection for automatic execution of suturing tasks in robotic minimally invasive surgery,” *IEEE Transactions on Automation Science and Engineering*, vol. 13, no. 2, pp. 552–563, 2016.
- [3] C. D’Ettorre, G. Dwyer, X. Du, F. Chadebecq, F. Vasconcelos, E. De Momi, and D. Stoyanov, “Automated pick-up of suturing needles for robotic surgical assistance,” in *2018 IEEE International Conference on Robotics and Automation (ICRA)*. IEEE, 2018, pp. 1370–1377.
- [4] P. Sundaresan, B. Thananjeyan, J. Chiu, D. Fer, and K. Goldberg, “Automated extraction of surgical needles from tissue phantoms,” in *2019 IEEE 15th International Conference on Automation Science and Engineering (CASE)*. IEEE, 2019, pp. 170–177.
- [5] Z.-Y. Chiu, F. Richter, E. K. Funk, R. K. Orosco, and M. C. Yip, “Bimanual regrasping for suture needles using reinforcement learning for rapid motion planning,” in *2021 IEEE International Conference on Robotics and Automation (ICRA)*. IEEE, 2021, pp. 7737–7743.
- [6] J. Xu, B. Li, B. Lu, Y.-H. Liu, Q. Dou, and P.-A. Heng, “Surrol: An open-source reinforcement learning centered and dvrk compatible platform for surgical robot learning,” in *2021 IEEE/RSJ International Conference on Intelligent Robots and Systems (IROS)*. IEEE, 2021, pp. 1821–1828.
- [7] A. Wilcox, J. Kerr, B. Thananjeyan, J. Ichnowski, M. Hwang, S. Paradis, D. Fer, and K. Goldberg, “Learning to localize, grasp, and hand over unmodified surgical needles,” in *2022 International Conference on Robotics and Automation (ICRA)*. IEEE, 2022, pp. 9637–9643.
- [8] F. Zhong, Y. Wang, Z. Wang, and Y.-H. Liu, “Dual-arm robotic needle insertion with active tissue deformation for autonomous suturing,” *IEEE Robotics and Automation Letters*, vol. 4, no. 3, pp. 2669–2676, 2019.

- [9] L. Han, H. Wang, Z. Liu, W. Chen, and X. Zhang, “Vision-based cutting control of deformable objects with surface tracking,” *IEEE/ASME Transactions on Mechatronics*, vol. 26, no. 4, pp. 2016–2026, 2020.
- [10] O. M. Andrychowicz, B. Baker, M. Chociej, R. Jozefowicz, B. McGrew, J. Pachocki, A. Petron, M. Plappert, G. Powell, A. Ray *et al.*, “Learning dexterous in-hand manipulation,” *The International Journal of Robotics Research*, vol. 39, no. 1, pp. 3–20, 2020.
- [11] D. Kalashnikov, A. Irpan, P. Pastor, J. Ibarz, A. Herzog, E. Jang, D. Quillen, E. Holly, M. Kalakrishnan, V. Vanhoucke *et al.*, “Scalable deep reinforcement learning for vision-based robotic manipulation,” in *Conference on Robot Learning*. PMLR, 2018, pp. 651–673.
- [12] D. Hafner, T. Lillicrap, J. Ba, and M. Norouzi, “Dream to control: Learning behaviors by latent imagination,” *arXiv preprint arXiv:1912.01603*, 2019.
- [13] D. Hafner, T. Lillicrap, M. Norouzi, and J. Ba, “Mastering atari with discrete world models,” *arXiv preprint arXiv:2010.02193*, 2020.
- [14] P. Wu, A. Escontrela, D. Hafner, K. Goldberg, and P. Abbeel, “Daydreamer: World models for physical robot learning,” *arXiv preprint arXiv:2206.14176*, 2022.
- [15] D. Ha and J. Schmidhuber, “World models,” *arXiv preprint arXiv:1803.10122*, 2018.
- [16] A. Nair, B. McGrew, M. Andrychowicz, W. Zaremba, and P. Abbeel, “Overcoming exploration in reinforcement learning with demonstrations,” in *2018 IEEE international conference on robotics and automation (ICRA)*. IEEE, 2018, pp. 6292–6299.
- [17] A. Munawar, J. Y. Wu, G. S. Fischer, R. H. Taylor, and P. Kazanzides, “Open simulation environment for learning and practice of robot-assisted surgical suturing,” *IEEE Robotics and Automation Letters*, vol. 7, no. 2, pp. 3843–3850, 2022.
- [18] H. Lin, B. Li, Y. Liu, and K. W. S. Au, “Open-source High-precision Autonomous Suturing Framework With Visual Guidance,” in *IEEE Int. Conf. Intell. Robots and Syst. (IROS) Workshop on “A Panacea Or An Alchemy? Benefits And Risks Of Robot Learning In Medical Applications”*, 2022.

APPENDIX I HYPERPARAMETERS

Name	Symbol	Value
Delta Translation	Δd	2mm
Delta Orientation	$\Delta \theta$	10°
Entropy Regularizer Weight	η	0.002
Actor Improvement Weight	η_a	1
BC Weight	η_{bc}	1
Virtual Clutch Timestep	H_{clutch}	6
Bounding Box Ratio	b	0.3
Batch Size	M	70
Batch Length	N	10
Imagine Horizon	H	15
Pre-training Steps	L_{pre}	100
Gradient Update	K	100
Gradient Update Step	L_{every}	50
World Model Learning Rate	l_ϕ	2×10^{-4}
Critic Learning Rate	l_ξ	4×10^{-5}
Actor Learning Rate	l_ψ	2×10^{-5}
RSSM Size	-	512